Space Sci Rev (2013) 175:165–182
DOI 10.1007/s11214-013-9979-4

# Fast Solar Wind Monitor (BMSW): Description and First Results

**Jana Šafránková · Zdeněk Němeček · Lubomír Přech · Georgy Zastenker · Ivo Čermák · Lev Chesalin · Arnošt Komárek · Jakub Vaverka · Martin Beránek · Jiří Pavlů · Elena Gavrilova · Boris Karimov · Arkadii Leibov**

Received: 4 September 2012 / Accepted: 19 March 2013 / Published online: 6 April 2013


**Abstract** Monitoring of solar wind parameters is a key problem of the Space Weather program. The paper presents a description of a novel fast solar wind monitor (Bright Monitor of the Solar Wind, BMSW) and the first results of its measurements of plasma moments with a time resolution ranging from seconds to 31 ms. The method of the fast monitoring is based on simultaneous measurements of the total ion flux and ion integral energy spectrum by six nearly identical Faraday cups (FCs). Three of them are dedicated to determination of the ion flow direction, whereas other three equipped with control grids supplied by a retarding potential are used for a determination of the density, temperature, and speed of the plasma flow. The paper introduces not only the measuring methods, the FCs design, and modes of operation, but brings the examples of time series of measurements and their comparison with the observations of other spacecraft as well as the first results of an analysis of frequency spectra of solar wind fluctuations within the ion kinetic scale, examples of rapid measurements at the ramp of an interplanetary shock and investigations of fast variations of alpha particle content.

**Keywords** Solar wind · Turbulence · Interplanetary shock

This work was supported partly by the Research plan MSM 0021620860 and grant ME 09106 financed by the Ministry of Education of the Czech Republic, and partly supported by the Czech Grant Agency under Contracts 205/09/0170 and 209/12/1774.

J. Šafránková (✉) · Z. Němeček · L. Přech · A. Komárek · J. Vaverka · M. Beránek · J. Pavlů
Faculty of Mathematics and Physics, Charles University, Prague, Czech Republic
e-mail: jana.safrankova@mff.cuni.cz

G. Zastenker · L. Chesalin · E. Gavrilova · B. Karimov · A. Leibov
Institute of Space Research, Russian Academy of Sciences, Moscow, Russia

I. Čermák
CGC Instruments, Chemnitz, Germany

## 1 Introduction

The past 40 years of solar-terrestrial relation research have shown that sudden changes of solar wind properties can significantly affect the state of Earth's magnetosphere. Accurate space weather forecasting requires spacecraft measurements of solar wind parameters with high temporal resolution and accuracy. These measurements have been difficult to obtain given the limitations on instrument weight and dimensions and on the telemetry bit rate.

Faraday's cups (FCs) have been used for space plasma investigations from the beginning of space exploration (Vasylinuas 1971). They have measured ion flux onboard Prognoz-type spacecraft in the solar wind (e.g., Gringauz et al. 1960, 1980; Zastenker et al. 1982; Šafránková et al. 1997) and in the plasmasphere (Vaisberg et al. 1979). The performance and capabilities of FCs have been extended by reducing their mass and power requirements (Lazarus et al. 1993). Aellig et al. (2001) showed that much faster measurements (0.7 s) of complete solar wind parameters were possible from 3-axis stabilized spacecraft. Kozák et al. (1985) used a set of FCs to determine the ion flow direction near the bow shock at high time resolution (62 ms). Avanov et al. (1984) used this method to measure ion flow fluctuations in the solar wind with a time resolution of 20 ms.

The FC systems mentioned above (on the spacecraft Intershock, Interball, and Prognoz–8) were designed for ultra fast measurements of the ion flux vector, however, other plasma parameters like density, speed, and temperature had a temporal resolution of 16–32 seconds. Since solar wind parameters vary over broad ranges and the direction of the bulk plasma velocity is generally unknown, multiple FCs or a FC with a segmented collector must be used to determine all the plasma parameters. A set of properly oriented FCs can provide the ion bulk velocity, the ratio of bulk to thermal velocity and the ion flux (Koval et al. 2005a, 2005b). Such measurements require knowledge of the velocity distribution which is obtained by sweeping a positive voltage on a control grid in front of the detector over the solar wind energy range (up to 3–5 kV) (e.g., Šafránková et al. 1997). The temporal resolution is limited to several seconds due to the limited frequency response of FC amplifiers.

The other possibility is a more complicated FC sensor with flux modulation produced by varying the potential on a control grid and selective current amplification at the modulation frequency (e.g., Ogilvie et al. 1995; Steinberg et al. 1996). The operating principle of the twin FC instruments used on WIND was discussed by Ogilvie et al. (1995) and new techniques to identify velocity and temperature uncertainties were developed in Kasper et al. (2006).

Measurements of the velocity distribution based on electrostatic analyzers and microchannel plates provide a similar resolution (e.g., McComas et al. 1998; Reme et al. 2001; McFadden et al. 2008). Nevertheless, fast measurements of the magnetic field and ion fluxes show that temporal resolutions of order of seconds are not sufficient to provide detailed understanding of solar wind dynamics and that a significant increase in time resolution is needed. This increase can be achieved if the full velocity distribution is narrow as observed; then velocity and temperature determinations can be made using data from only a few (usually 3–6) energy windows (e.g., Zastenker et al. 2000).

Based on this history, a fast solar wind monitor must have: (1) sensors pointed approximately into the solar wind flow direction which requires either that the spacecraft rotational axis is pointed toward the Sun (like a Russian Prognoz-type spacecraft) or a three-axis stabilized apparatus with a dedicated platform (Aellig et al. 2001); (2) Elimination of voltage sweeping on a control grid requires parallel measurements from several sensors (Galeev et al. 1986); (3) A determination of basic solar wind parameters (density, three velocity

components, and temperature) supposes five independent readouts (i.e., five data points); (4) The power spectral density of the solar wind turbulence at the upper end of the ion kinetic scale is expected to be up to ten orders of magnitude lower than that at the beginning of the MHD scale ($\approx 10^{-5}$ Hz), thus the amplitude of fluctuations should exceed the instrumental and statistical noises. This requires sufficiently large geometrical factors for all sensors.

This paper presents a design of a solar wind monitor that fulfils all these requirements and is based on six independent FCs. Three FCs point toward the Sun to determination the speed, density, and temperature from three points of the velocity distribution function, the other three FCs point at angles deflected from the solar direction to determine the ion flow direction. If a Maxwellian distribution is assumed, this configuration can determine the density, temperature, and full solar wind velocity vector with a time resolution up to 0.31 ms.

## 2 Spektr-R and Its Scientific Objectives in the Solar Wind

The Spektr-R spacecraft, which was launched on July 18, 2011 from the Baikonur facility, provides a unique opportunity to measure plasma parameters in the solar wind because its orbital parameters are as follows: a period of 8.2 days, apogee—333 570 kilometers, and perigee—576 kilometers. The spacecraft is located in the solar wind for 7–8 days per orbit which provides a nearly continuous monitoring of solar wind conditions. Although Spektr-R was designed as an astrophysical mission, it also carries the Plasma-F package. This package (1) monitors the interplanetary medium for to support space weather studies and forecasts; (2) studies solar wind turbulence; (3) investigates energetic particle acceleration processes; and (4) measures the fine structure of solar wind disturbances. The package consists of the MEP energetic particle spectrometer, a magnetometer, and the BMSW solar wind monitor which is described here.

## 3 BMSW Design and Operational Modes

The constrains listed above led to the development of a small fast solar wind monitor based on simultaneous measurements of a set of Faraday's cups. The location of the instrument on the solar panel eliminates the dedicated platform but it requires an additional determination of its exact orientation with respect to the Sun because the attitude of the solar panel is provided with an accuracy of $\approx \pm 10^{\circ}$ only. The fast speed of measurements is reached by two different working modes described in the next section. The monitor is designed to measure ion moments in all environments that can be encountered in the solar wind: pristine high- or low-speed solar wind, CIRs (Corotating Interaction Regions), ICMEs (Interplanetary Coronal Mass Ejections), IP (Interplanetary) shocks irrespective their drivers, the sheaths behind the shocks, etc. An application of such monitor is limited by two basic factors: (1) the electron temperature below $\approx$100 eV (this condition is fulfilled in the solar wind and in the whole magnetosheath except a narrow subsolar region), and (2) the angular aperture of FCs. We will discuss these conditions further in the text.

### 3.1 Geometry of BMSW Faraday's Cups

The idea of the Faraday cup is simple and straightforward, however, a lot of problems should be solved prior to its application for a fast solar wind monitor. A schematics of the used FC

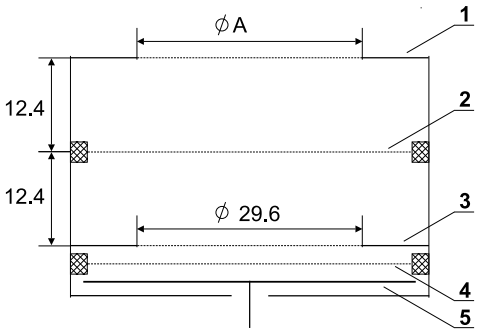


**Fig. 1** A design of the Faraday cup: (1) and (3) are outer and inner diaphragms with grounded grids, respectively; (2) a positive control grid, (4) a suppressor grid, (5) a collector. The diameter marked as $A$ is 20 mm for FCs of the energetic section, whereas $A = 30$ mm is used for FCs of the angular section

design is shown in Fig. 1. The FC is equipped with four grids: grounded grids cover outer and inner diaphragms (1, 3) that define the angular characteristics; a positive control grid (2) is placed at an equidistance from outer and inner diaphragms; and a suppressor grid (4) lies between the inner diaphragm and a collector (5). The grounded grids are used for an elimination of the internal electric field outside FC.

The control grid is connected to a tunable HV source and thus only the ions with the velocity sufficient to overcome the grid potential can reach the collector. The suppressor grid is powered by a negative potential of $\approx -300$ V. This potential returns back photoelectrons emitted from the collector by a solar UV radiation as well as solar wind electrons. The value of the suppressor grid potential is sufficient for precise measurements in a plasma with the electron temperature up to $\approx 100$ eV. The electron component of the collector current caused by photoelectrons from the suppressor grid should be subtracted from the total measured current. This point is crucial for a precise determination of solar wind parameters because preliminary estimations confirmed by an in-flight calibration (see Sect. 3.5) has shown that this photocurrent is roughly equivalent to the proton number flux of the order of $10^7$ cm$^{-2}$ s$^{-1}$, i.e., about 10 % of the nominal solar wind flux.

A geometry of an individual FC should provide a measurable ion current for all possible angles of incidence and in a full range of expected plasma parameters. We assume that the ion flow can be deflected from the antisunward direction by 20° and the monitor itself can be oriented toward the Sun with an accuracy of $\approx 10°$. Another $\approx 10°$ deviation should be added because a typical ratio of thermal and bulk velocities is 0.1 and thus, the angular characteristics of FC should fall to zero at least at $\approx 50°$.

It can be easily shown (Koval et al. 2005a, 2005b) that the characteristics of FCs are self-similar for a constant ratio of thermal and bulk velocities, $K$. A determination of the solar wind parameters can be thus divided into two particular tasks: (1) the estimation of the total ion flux vector and $K$; and (2) the determination of the speed and temperature. These two tasks assume slightly different FC geometries because a linear dependence of the FC current on the angle between the ion flux vector and FC axis would be appropriate for the first task, while a constant FC current in a broad range of these angles would simplify the second task. The shape of the angular characteristics depends on a ratio of diameters of outer and inner diaphragms for a fixed $K$ (see Fig. 1).

Figure 2 shows these characteristics (the dependence of the normalized FC current on the incidence angle, $\alpha$ for different values of $K$) for two geometries used in the BMSW instrument; the geometry applied for the velocity direction determination (hereafter referred as FC3) is shown in Fig. 2a and that used for the estimation of the bulk and thermal speeds (hereafter FC0) in Fig. 2b. The vertical axis presents a FC collector current, $J$ normalized to the current corresponding to the flux aligned with the FC axis, $J_0$. The characteristics of the

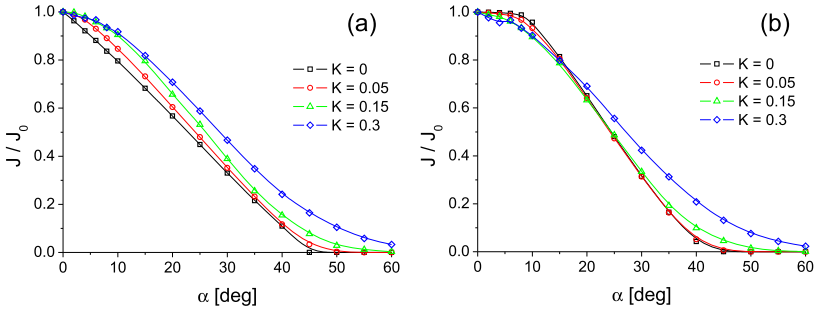


**Fig. 2** Angular characteristics of both FC geometries; (**a**) the FC3; and (**b**) FC0 types, respectively for different thermal to bulk speed ratios, $K$. The *black curves* ($K = 0$) show the characteristics for a parallel ion beam

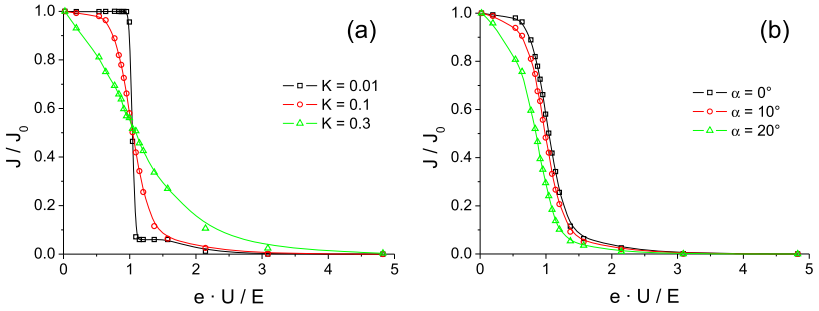


**Fig. 3** FC energetic characteristics—normalized FC current, $J/J_0$ as a function of the normalized grid potential, $eU/E$: (**a**) the dependence on the $K$ ratio; (**b**) the dependence on the $\alpha$ incidence angle for $K = 0.1$

FC3 geometry (Fig. 2a) are almost linear through a whole range of the angles of incidence and the dependence on the ion temperature is monotonous. On the other hand, for the FC0 geometry (Fig. 2b), a flat angular characteristics is desirable. This can be simply achieved by decreasing of the entrance window diameter (diaphragm (1) in Fig. 1). The characteristics can be then described as cosine of the incidence angle for small $K$. We use FCs with entrance windows decreased to 20 mm that exhibit a flat angular characteristics up to $\approx 10°$ from the FC axis (Fig. 2b).

The determination of the solar wind speed and temperature is based on the energetic characteristics of FC0 that are measured by a sweeping voltage applied on the control grid. Since the shape of the characteristics is determined by a ratio of the solar wind bulk energy, $E = \frac{1}{2}mV^2$ and the potential applied on the FC grid, $U$ for a given $K$, Fig. 3 shows normalized FC collector currents, $J/J_0$ as a function of the $e.U/E$ ratio ($e$ is the elementary charge). Figure 3a was computed under an assumption of the bulk velocity oriented along the FC axis and illustrates the changes of FC characteristics with the $K$ ratio, whereas the characteristics for $K = 0.1$ and different declinations of the bulk velocity from the FC axis are shown in Fig. 3b.

The characteristics were computed using the ion trajectory tracing within a FC by the SIMION software package. The FC geometry used in these calculations reflects all problems discussed in Šafránková et al. (2008) like diameters of the grid wires, grid wire spacing and finite FC dimensions. In simulations, the input ions were protons with an addition of 3 % of alpha particles with a thermal speed equal to that of protons.

The black points in Fig. 3a represent the characteristics computed for a ratio of bulk and thermal speeds, $K = 0.01$ and shows the influence of the control grid wire spacing. In an approximation of a constant potential in the grid plane, the characteristics would fall to a level corresponding to alpha particle content at $eU/E = 1$ and the slope would be much steeper. However, the decrease of the potential among grid wires leads to a more gradual decrease of the FC current and to a shift of the steep part toward higher values of $eU/E$. This is important because the slope can be clearly identified and used in the data processing.

A part of the characteristics between $J/J_0 = 0.7$ and $J/J_0 = 0.3$ is nearly linear and thus the slope can be determined from any part of the characteristics in this range with a sufficient accuracy. Another interesting feature is that all characteristics intersect at about $J/J_0 = 0.5$, thus $eU/E$ corresponding to this current ratio can be used for a rough estimation of the solar wind speed.

The influence of alpha particles on the characteristics is notable if the temperature is low ($K < 0.1$). Under these conditions, alpha particles can be separated and processed but they cannot be distinguished from energetic protons for larger temperatures. However, all spectrometers without a mass selection suffer with the same problem.

Figure 3b demonstrates a dependence of the FC energetic characteristics on the angle between the solar wind velocity and FC axis for a typical ratio of the thermal and bulk speeds, $K = 0.1$. The slope of the energetic characteristics is nearly unaffected by the incidence angle, whereas the location of a falling part on the energetic scale roughly follows the cosine law. This effect is connected with the electric field of the control grid that affects only the velocity component aligned with the FC axis.

### 3.2 BMSW Design

As noted above, assuming the isotropic Maxwellian distribution of solar wind protons, we should determine 5 parameters for its full description—density, three components of velocity vector (or speed and two direction angles), and temperature—and thus, five independent measurements are required. This implies a minimum set of five FCs. We have chosen a configuration with six FCs divided into two groups: in the first of them, three FCs are oriented along the X axis of the instrument (i.e., approximately toward the Sun), while three FCs of the other group are inclined by 20° from the instrument X-axis.

The second (so-called angular) section uses the FC3 geometry that is more sensitive to the declination of the bulk flow from the instrument axis. Consequently, this group of FCs serves mainly for a determination of the solar wind direction and the control grids of these FCs are grounded.

Three FCs of the so-called energetic section are oriented toward the Sun and they are equipped with HV sources that supply the control grid of each particular FC. These FCs use the FC0 geometry and work in two basic configurations, hereafter denoted as sweeping and adaptive modes.

The both sections of FC sensors can be distinguished in a photo of the BMSW engineering model (Fig. 4). The axes of FCs of the energetic section are oriented perpendicularly to the instruments base and the axes of FCs of the angular section are declined from this direction and create an equilateral triangle.

### 3.3 Sweeping Mode

In the sweeping mode, the voltages of FCs of the energetic section are swept linearly between 0.1 and 3 or 3.75 kV up and down, and thus these FCs measure the energy distribution


**Fig. 4** A photo of the engineering model

shown in Fig. 3. A duration of the sweep can be set as 1.5, 3 or 6 s by the control command from the ground. Since the phase of triangular voltages of the three FCs are shifted by 120°, the resulting time resolution varies from 0.5 to 2 s. An example of the raw data transmitted to the Earth in the sweeping mode is shown in Fig. 5a. HV0, HV1, and HV2 are the voltages supplying the control grids of the FCs of the energetic section; FC0, FC1, and FC2 are currents of corresponding FCs (in arbitrary units). FC3, FC4, and FC5 are currents of three FCs of the angular section (without the voltage on the control grids). The differences among FC3, FC4, and FC5 currents serve for a determination of the velocity direction, whereas the energetic characteristics that are shown in Fig. 5b are used for an estimation of the speed and temperature. This figure is a blow-up of the second panel of Fig. 5a for one sweep with the time scale converted into the voltage. Note that we use a logarithmic scale in both panels in Figs. 5b and 5c.

As it can be seen in Fig. 5b, the proton and alpha particle parts of the characteristics can be clearly resolved in this case. In order to show the abilities of the device, we have chosen the time interval with a very low alpha particle content, less than 1 %. Although it was not expected in the experiment design, the alpha/proton density ratio can be computed either from the current profile in Fig. 5b, or from the derivative of the energetic characteristics shown in Fig. 5c. However, both these methods have some limitations. The FC current is proportional to a sum of fluxes of different ion species multiplied by their charge and thus we should assume that the speeds of all species are equal. We believe that it is a reasonable assumption for the solar wind. On the other hand, the ratio of peaks in the profiles of the energetic characteristic derivative (Fig. 5c) depends on the temperatures of protons and alpha particles that can vary in broad ranges. For this reason, we use the ratio of the FC currents at present. Nevertheless, we believe that we will be able to determine the alpha particle speed and temperature in future but this task requires a further modeling effort.

We would like to note that this mode was slightly modified in course of the experiment. One of HV sources is permanently switched off for the determination of the full current and only two others are supplied with the sweeping voltage. The reasons will be discussed in the Sect. 3.5. The sweeping mode thus currently provides a 1-D distribution function of solar wind ions and a direction of the velocity with the time resolution up to 0.75 s.

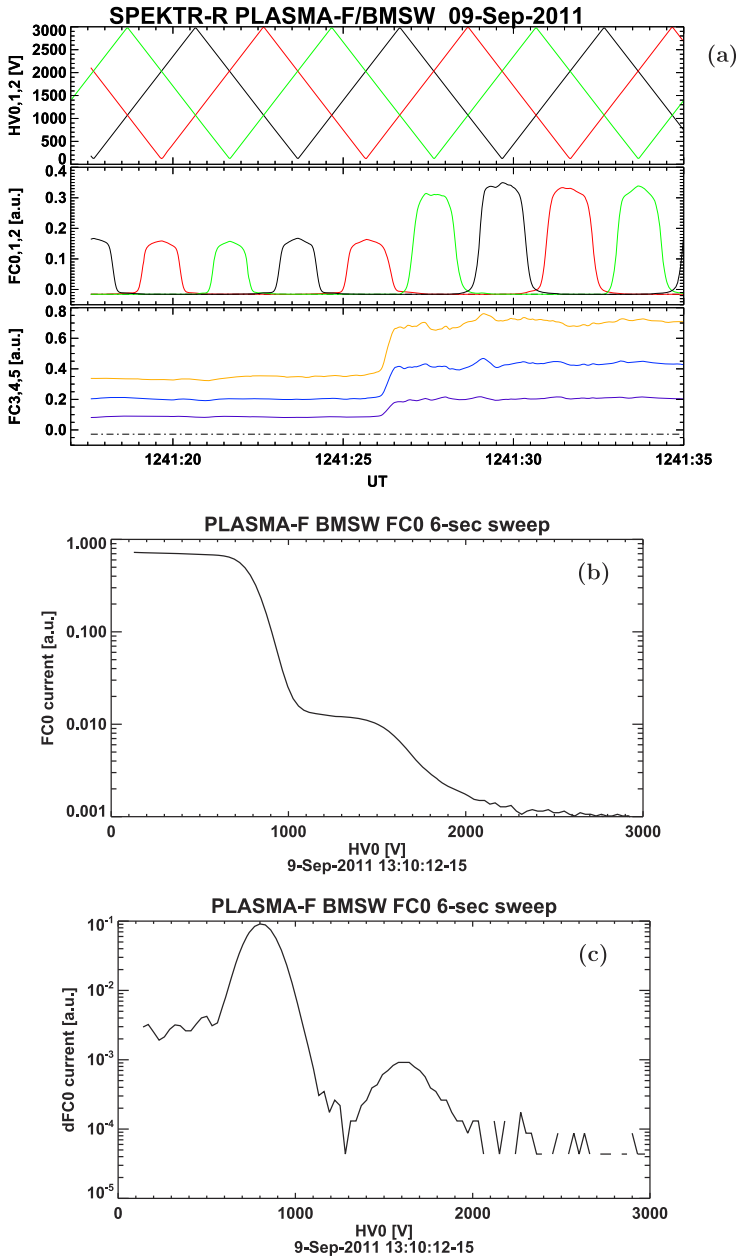


**Fig. 5** (**a**) An example of a 20 s raw data transmitted to the Earth in the sweeping mode on September 9, 2011; (**b**) an example of measured energetic characteristics; (**c**) the derivative of the energetic characteristics to computation of the alpha-particle/proton density ratio. In the *top panel*, the colors stand for different FCs: FC0—*red*, FC1—*black*, FC2—*green*, FC3—*yellow*, FC4—*dark blue*, FC5—*light blue*, and different HV: HV0—*black*, HV1—*red*, and HV2—*green*

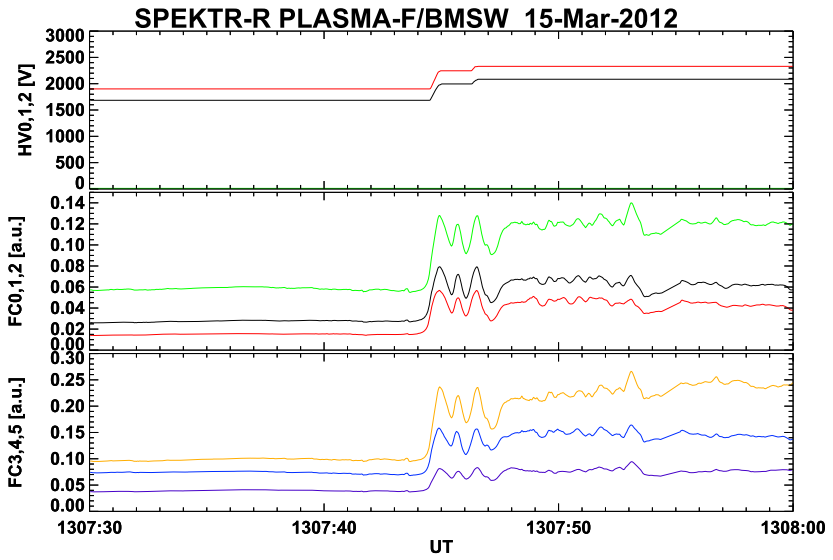


**Fig. 6** An example of the raw data measured in the adaptive mode across the IP shock on March 15, 2012. The colors stand for different FCs: FC0—*red*, FC1—*black*, FC2—*green*, FC3—*yellow*, FC4—*dark blue*, FC5—*light blue*, and different HV: HV0—*black*, HV1—*red*, and HV2 = 0

### 3.4 Adaptive Mode

In the adaptive mode, one FC of the energetic section is chosen as the leading one and its HV source is switched off. The feed-back loops adjust the voltages of two other sunward looking FCs to depress their collector currents to preset fractions of the collector current of the leading FC. The values of 0.3; 0.5; and 0.7 were chosen in accord with the energetic characteristics in Fig. 2 and the actual used value is set from the ground. For a standard operation, the ratios 0.3 and 0.7 are preset and these FCs provide three points of the distribution function with a full time resolution of 31 ms. To achieve this time resolution, the feed-back loops should keep the preselected ratios of FC currents even under abrupt changes of solar wind parameters.

An example of the raw data measured in the adaptive mode across an IP shock is shown in Fig. 6. Although the solar wind speed (determined in course of further data processing) changed from 500 to 650 km/s within less than 0.5 s, the feed-back loops are able to adjust voltages on the control grids (HV0 and HV1 in the top panel, HV2 is set to zero) to the values that keep the ratios of currents, $FC0/FC2$ and $FC1/FC2$ within the range of 0.3–0.7, thus the plasma parameters can be determined in each point, i.e., with a full time resolution. It should be noted that in order to avoid oscillations of the feed-back circuits, the HV ramps are limited to 2 kV/s and a band of insensitivity around target ratio values (0.3 or 0.7) is introduced, so the exact ratios are within a 0.25–0.75 interval. Prior to calculations of ratios, the estimated photocurrent (set by a command from the ground) is subtracted from the FC currents.

Last but not least, we should mention that this time resolution is appropriate for the analysis of the spectral properties of solar wind turbulence up to ≈16 Hz. To avoid aliasing, the FC amplifiers are followed by the Bessel type low-pass filters of 6th order adjusted to the Nyquist frequency and all signals are transmitted to the Earth with a 16 (or 24) bit resolution in order to depress the quantization noise.

### 3.5 In-flight Calibration and Data Processing

Although all parts of the instrument were carefully tested and calibrated prior to the flight, the in-flight calibration is necessary to determine a level of photocurrents and to account for aging of different components. The most important part of this calibration is a determination of photocurrents that depends on the orientation of a particular FC with respect to the Sun and on the time. We apply two ways of its determination: (1) the spacecraft periodically crosses magnetospheric lobes where the photocurrent is the only component of the collector current and it could be estimated and later subtracted from a total measured current, and (2) to slow down solar wind ions completely by a high (≈3 kV) potential on the control grid. Such calibration requires periods of a slow solar wind (≈300 km/s) which are rather frequent (Zastenker et al. 2000).

The latter technique is applicable only to FCs equipped with the HV sources and it is performed daily, whereas the former procedure can be used for all FCs but once per orbit only. Nevertheless, a year of operation allowed us to determine both the angular and time dependences that are used for the data processing.

The inter-calibration of amplifiers and AD converters is performed permanently for FC0, FC1, and FC2 and the results did not reveal any changes. This fact is principal for FC3, FC4, and FC5 because they have different orientations and their inter-calibration is difficult because they never measure the same currents.

The output of the device basically consists of two types of frames. Both of them contain the internal time, 6 FC currents, 3 voltages applied on control grids, information about a declination of the instrument main axis from the direction to the Sun, and technical information on the mode, temperatures of amplifiers, etc. The full resolution frames contain the FC currents and control grid voltages with a full time resolution, whereas the data are averaged over preselected intervals in the reduced (so-called compressed) frames. Both types of frames are stored in the on-board memory and transmitted to the Earth on request. The volume of the onboard memory is sufficient for about one year of continuous measurements. It leaves enough time for processing of the reduced frames and an identification of interesting time intervals that are then transmitted with the full time resolution.

A first step of the ground data processing is a determination of the photocurrents and calibration constants that were described in the previous sections. After an application of the corrections to raw data, the plasma moments are calculated. Let us assume that $n$ is the proton number density, $V$ is the speed, $K$ is a ratio of the thermal and bulk speeds, and $\theta$ and $\phi$ are cone and clock angles of the solar wind speed in the instrument frame of reference, respectively. The angles between the solar wind velocity and FC axes, $\alpha_i$ can be expressed from $\theta$ and $\phi$ by the following way:

$$\begin{aligned} \alpha_i &= \theta \qquad\qquad \text{for } i = 0, 1, 2 \\ \alpha_i &= \alpha_i(\theta, \phi) \quad \text{for } i = 3, 4, 5 \end{aligned} \tag{1}$$

In this notation and assuming zero potential of the control grid, we can write the FC current densities, $J_i$ as:

$$J_i = enVf_j(\alpha_i, K) \quad \text{for } j = 0, 3 \tag{2}$$

where $f_j$ are functions defined by the FC geometry, and $e$ is the elementary charge. There are 4 unknown variables: product $nV$, $\theta$, $\phi$, and $K$, thus 4 independent readouts are required for their determinations. We use currents of three declined FCs (FC3, FC4, FC5) and complement them with the FC from the energetic section that is without the voltage on the control grid (usually FC2). The functions $f_j$ were estimated as the best polynomial fits of

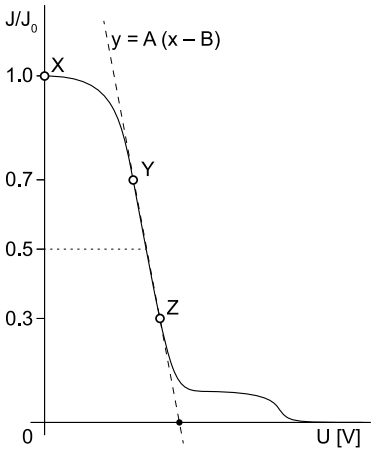


**Fig. 7** A sketch of estimation of the solar wind velocity from the measured energetic characteristics. For explanation see the text

the fourth order in both variables, $\alpha$ and $K$ to the model characteristics discussed in the Sect. 3.1. A numerical solution of the above described set of equations yields $nV$, $\theta$, $\phi$, and $K$. We will call the value of $K$ determined by this way as $K_1$ for reasons explained below.

For an estimation of the velocity, we introduce two auxiliary variables—$A$ and $B$. $A$ is defined as the first derivative of the energetic characteristics (Fig. 3) at a point where the FC current is approximately equal to one half of the current corresponding to a zero potential of the control grid:

$$A = \frac{\mathrm{d}(J/J_0)}{\mathrm{d}U}\Big|_{J/J_0=0.5} \tag{3}$$

This derivative is approximated with a linear fit of 5 nearest points of the measured characteristics in the sweeping mode or calculated from two points measured in the adaptive mode as it is illustrated in Fig. 7. This figure shows the normalized FC current density, $J/J_0$ as a function of the voltage, $U$ applied on the control grid of FC. Such curve is obtained in the sweeping mode, whereas only points marked as $X$, $Y$, and $Z$ are measured in the adaptive mode. The dashed thin line has the slope $A$ and is coming through the point $J/J_0 = 0.5$. The intersection of this line with the horizontal (voltage) axis defines the second auxiliary variable $B$.

Simple physical considerations lead to the conclusion that the main factor influencing the slope of the energetic characteristics would be the ion temperature, whereas both the ion speed and temperature affect the position of $B$. However, the planar geometry together with a limited angular aperture of FCs cause a dependence of both $A$ and $B$ on an incidence angle, $\theta$. Based on an analysis of the modeled FC characteristics under different input conditions, we can write the simplified equations:

$$\begin{aligned} A &= \frac{1}{E} g(K_2, \theta) \\ B &= E h(K_2, \theta) \end{aligned} \tag{4}$$

where $E = 1/2mV^2$ ($m$ is the proton mass) and the functions $g$ and $h$ were determined as the best polynomial fit to simulated FC characteristics. Note that we mark the ratio of thermal to bulk speeds as $K_2$ in these equations. Since the angle $\theta$ is known from the procedure described above, the numerical solution of these equations provides the values of $E$ and $K_2$,

and thus the ion speed and temperature. The analysis has shown that the second order fit is sufficient to reach a speed accuracy better than $10^{-2}$ in the ranges of expected solar wind or magnetosheath parameters.

As we already noted, we have six independent readouts from FCs for a determination of five variables. Consequently, our procedure provides two values of $K$—$K_1$ and $K_2$ that would be equal but there are small differences caused by instrumental and plasma noises and a slight imprecision in manufacturing of FCs. This difference does not exceed 10 % in the data processed up to now. Since the dependence of $A$ and $B$ on the value of $K$ is much stronger than the dependence of the FC currents in Eq. 2, we prefer the value of $K_2$ obtained from Eqs. 3 and 4.

## 4 Preliminary Results

In this part, we present a few cases of the first interesting observations. An example of measurements of solar wind parameters by BMSW and their comparison with simultaneous observations of Wind and Themis B on October 25, 2011 is shown in Fig. 8. We present only the best available time resolution data for this plot (BMSW works in the adaptive mode), thus Themis B measurements cover only a part of the interval shown in the top panel. However, taking into account the spacecraft locations, Wind (260; 62; 15) $R_E$, Themis B (55; −20; −5) $R_E$, Spektr-R (−10; −47; +15) $R_E$, one would expect a better agreement of Spektr-R observations with those of Themis B and it is the case as it can be seen in the top panel. However, particular features observed by Spektr-R were registered by Wind, whereas they are missed in Themis B high-resolution data (e.g., a density enhancement at ≈1615 UT).

The blow-up of 15-minute measurements in the middle panel reveals still a very good overall agreement of the parameters of all spacecraft but neither Wind nor Themis B plasma spectrometers can resolve the high-frequency fluctuations of all quantities that are clearly seen within one-minute interval in the last panel.

### 4.1 Oscillations Associated with an Interplanetary Shock

Figure 9 presents the changes of plasma parameters observed across the interplanetary (IP) shock observed on March 15, 2012 near the dusk bow shock ((−2; 22; 23) $R_E$ in GSE coordinates) at ≈1308 UT. The figure shows 6 seconds of density, velocity, and temperature measurements that were derived from the raw data presented in Fig. 6. The cadence of measurements is highlighted by the crosses in the density (top) panel. Although the density changed by a factor of 2 and the speed jumps from 520 to 650 km/s, the shock exhibits a laminar structure with smooth changes of all parameters at the shock ramp that lasts about 400 ms. Since the Spektr-R magnetometer is not in operation, we use the Themis B observations as a proxy of the interplanetary magnetic field at our location. Themis B observed the same IP shock near the dawn bow shock ((5; −55; −12) $R_E$) at ≈1310 UT. A combination of our plasma measurements with the Themis B magnetic field yields the shock normal $n = -0.92; -0.34; -0.2$ and speed 724 km/s. These parameters are consistent with the timing of Themis B/Spektr-R IP shock observations.

The shock ramp thickness computed from the shock speed is as thin as 250 km, i.e., about one third of the upstream proton gyroradius. This finding is in an agreement with the estimations made by Schwartz et al. (2011) that were based on an analysis of Cluster electron measurements. However, there is one very important difference. Schwartz et al.

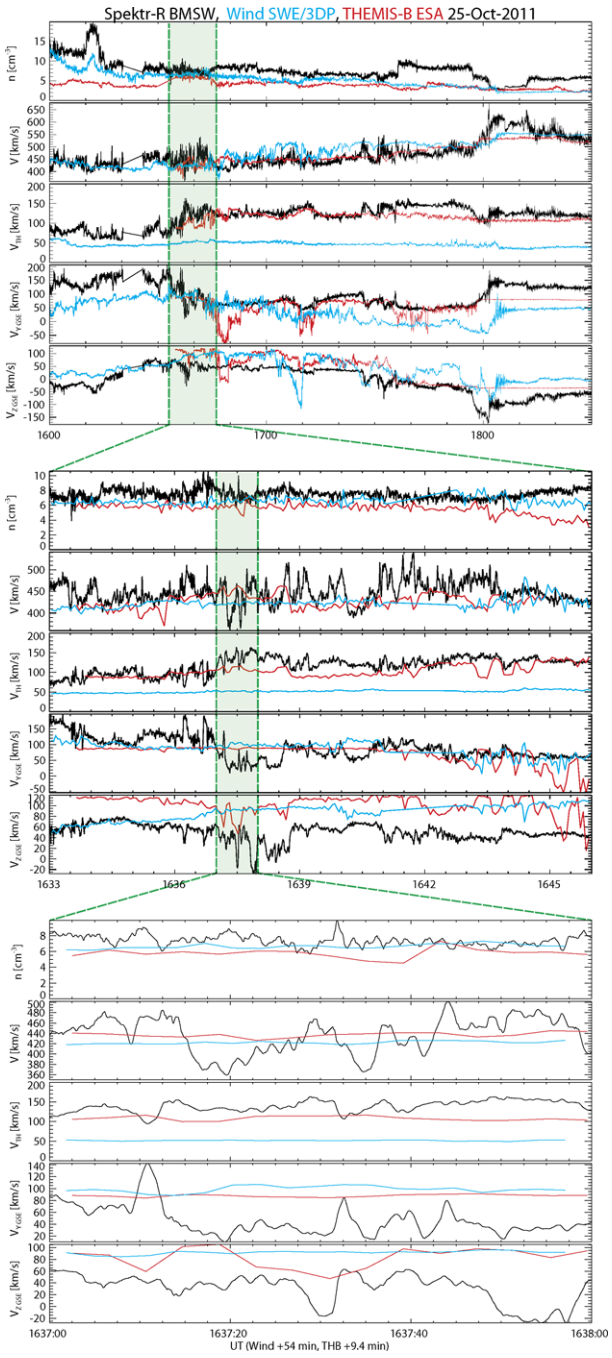


**Fig. 8** The time series of joint measurements of solar wind parameters by Spektr-R (BMSW, 31 ms resolution), Wind (3DP, 3-s resolution), and Themis B (ESA, 4-s resolution) on October 25, 2011 between 1600 and 1830 UT in three time intervals. In each panel, from top to bottom: the density, $n$; the solar wind velocity, $V$, the thermal velocity, $V_{th}$; and two velocity components, $V_{Y\,GSE}$ and $V_{Z\,GSE}$, respectively

(2011) reported an electron heating within the bow shock ramp occurring on the scale of several electron inertial lengths but our observations show the ion heating that is completed within one or two ion inertial lengths. An additional theoretical effort is required to explain such rapid ion heating.

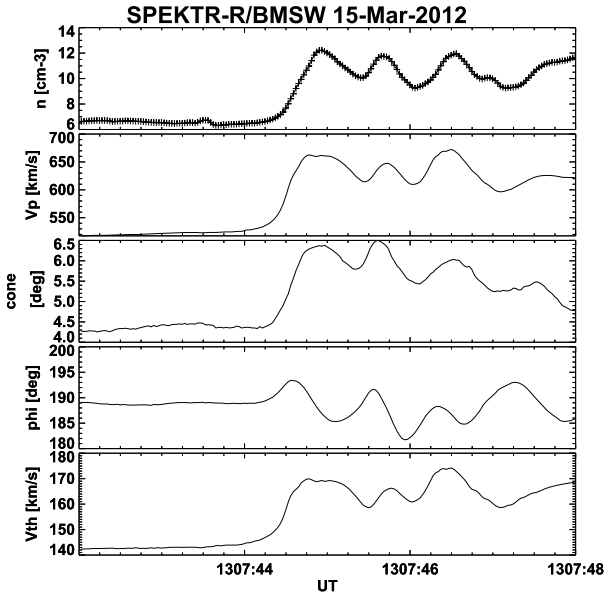


**Fig. 9** An example of computed parameters of the IP shock shown in Fig. 6 measured in the adaptive mode on the 6-s time interval. From top to bottom: the proton density, $N_p$, proton speed, $V_p$, two angles, and thermal velocity, $V_{th}$

The ramp is followed by a train of oscillations with the frequency ≈1.25 Hz in the spacecraft frame. In-phase changes of the velocity magnitude, temperature, and density and only weak variations of the velocity direction suggest a magnetosonic origin of these oscillations but a more precise determination of their mode is difficult without simultaneous magnetic field measurements. However, these oscillations are damped within 6 s after the shock ramp. Since possible waves generated by the shock cannot probably reach the spacecraft, we suppose that the observed oscillations are connected with the shock spatial structure that is swept along the spacecraft. In such a case, its typical dimension would be of the order of proton gyroradius (700 km). Similar structures in the magnetic field were reported by Balikhin et al. (2008) at the Venus bow shock or by Kajdic et al. (2012) at an IP shock and attributed to a standing wave associated with the IP shock.

### 4.2 Spectra of the Solar Wind Turbulence

The Voyager mission revealed nearly isothermic expansion of the solar wind along a whole path to the termination shock and thus the question on the source of an additional heat arises. Since the gradual dissipation of the energy stored in the chaotic component of the solar wind motion is the most probable source, a study of the solar wind turbulence is one of the principal problems of the present space physics (Podesta et al. 2006). Fast measurements of the interplanetary magnetic field revealed that its frequency spectrum can be divided into several frequency domains. Within each of them, the spectrum shape can be described by a power law but the exponents are different. The spectral slope of 5/3 was found in the so-called MHD regime (≈$10^{-5}$–$10^{-1}$ Hz), whereas a steeper slope (about −3) is typical for the ion kinetic scale(≈$10^{-1}$–$10^{2}$ Hz). There are some suggestions on further steepening of the spectrum at higher frequencies where the turbulence is driven by the electron kinetics (Chen et al. 2012). Due to a time resolution of the present onboard spectrometers, the plasma turbulence within the MHD scale is rather well understood but the kinetic scale was accessible only indirectly using the spacecraft potential or electric

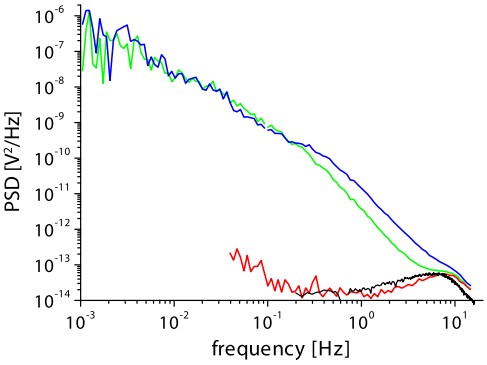


**Fig. 10** Power spectral densities of the amplifier noise determined during tests (*black*); and on the orbit (*red*); and their comparison with power spectral densities of collector currents of the FC with (FC1—*green*) and without (FC2—*blue*) deceleration potential on the control grid

field measurements as a proxy of the plasma density or velocity (e.g., Bale et al. 2005; Chen et al. 2011, 2012).

The time resolution of the BMSW instrument is sufficient for a spectral analysis of all basic plasma parameters up to 16 Hz, i.e., to the ion kinetic scale. However, a fluctuation level at high frequencies is low and thus the question of the noise connected with the measuring technique is of a principal importance. The measurement of all parameters is based on the currents of FCs, thus we will start with an analysis of their noise. Figure 10 compares four different measurements. The measurements of the frequency spectrum of the FC amplifier noise were done in the laboratory (black) through testing. The red curve shows the spectrum of the noise determined on the orbit during an interval of the photocurrent calibration. As described above, the particle component of the FC current is terminated by the high voltage applied on the control grid in course of this calibration and fluctuations of the photocurrent can be neglected. We can see that black and red curves are nearly identical. It means that the instrument and/or spacecraft systems do not add any notable component to the noise of the amplifier.

The blue and green curves in Fig. 10 show the frequency spectra of two FCs in a standard adaptive working mode. These spectra were computed through the interval 1500–1730 UT on November 10, 2011 that exhibited moderate fluctuations of the solar wind parameters. One can clearly identify the MHD (below $\approx$0.3 Hz) and steeper kinetic parts of the spectra. However, although the blue spectrum decreases with the frequency nearly continuously, the green spectrum exhibits a plateau above $\approx$3 Hz. The green spectrum belongs to FC1 with a voltage on the control grid that keeps its current at a level of 30 % of FC2 (blue spectrum). The lower fluctuation level of the FC1 current does not allow to distinguish its fluctuations from the instrumental noise above 3 Hz. Since the currents of FCs with the voltage on control grids are used for the measurements of the temperature and speed, the same should be applied on these quantities. Nevertheless, our analysis of a large number of intervals has shown that a noise effect does not prevent the reliable determination of the spectral indices in the ion kinetic scale even during very quiet solar wind intervals.

A sample of the power spectra of the density, velocity, and thermal speed are shown in Fig. 11 where a 5-hour interval of BMSW measurements in the adaptive mode on April 23, 2012 is analyzed. Inspection of the figure indicates that the power spectra of all parameters contain two parts differing by their slopes. The red lines distinguish the parts of the spectra used for the slope determination, their values are given in the figures. The slopes of the low-frequency parts range from $-1.35$ for the speed to $-1.48$ for the density, i.e., they are on average a slightly lower than expected $-5/3$. The slopes of the bulk and thermal speeds are close to already discussed $-3/2$ (e.g., Salem et al. 2009; Podesta and Borovsky 2010;

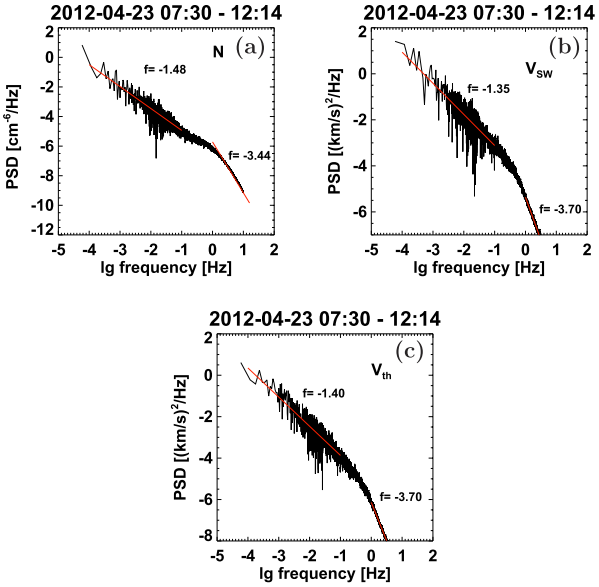


**Fig. 11** Examples of power spectra of the ion density, $N$ (**a**); total ion velocity, $V_{SW}$ (**b**); and thermal ion speed, $V_{th}$ (**c**) on April 24, 2012 between ≈0730 and 1214 UT

Wicks et al. 2011). However, as analyzed in Šafránková et al. (2013), the slopes vary in a broad range. On the other hand, the slopes of all parameters at the high-frequency part range from −3.44 for the density to −3.70 for the speed and thermal speed, i.e., they are much steeper than those in the MHD range. A careful examination of the density spectrum in Fig. 11 shows a slight flattening at the high-frequency end of the MHD scale (0.1–0.5 Hz). This feature was already reported and attributed to the compressive turbulence (e.g., Hollweg 1999).

### 4.3 Variation of the He Abundance in the Solar Wind

The ratio of the alpha particle and proton densities is an indicator of the source of the currently observed solar wind stream. It is known that the average He abundance depends on the solar cycle being about 4 % in the maximum and varying between 1–4 % through the solar minimum. These variations are connected with a dependence of the average He abundance on the solar wind speed (He abundance rises with the speed, Kasper et al. 2007). The authors attributed the variable abundance to the different proportions of two sources (streamer belt and active regions) during the averaging periods. The close connection of the He abundance with solar activity is further supported with observations of interplanetary coronal mass ejections that are often highly enriched in helium and values of 15–20 % were reported.

A preliminary analysis of the BMSW data acquired in the sweeping mode shows that the He abundance can rapidly vary over much shorter time scales. Figure 12 shows approximately 9 hours of continuous measurements of the dense and moderately fast solar wind. The speed is nearly constant but the He abundance (the last panel of the figure) varies between 4–10 %. An IP shock driven by a halo CME (Coronal Mass Ejections) was observed ≈30 hours prior to the depicted interval and thus the overall enhancement of the He abundance is probably connected with this event. However, the sources of its large variability would be determined in course of a further data evaluation.

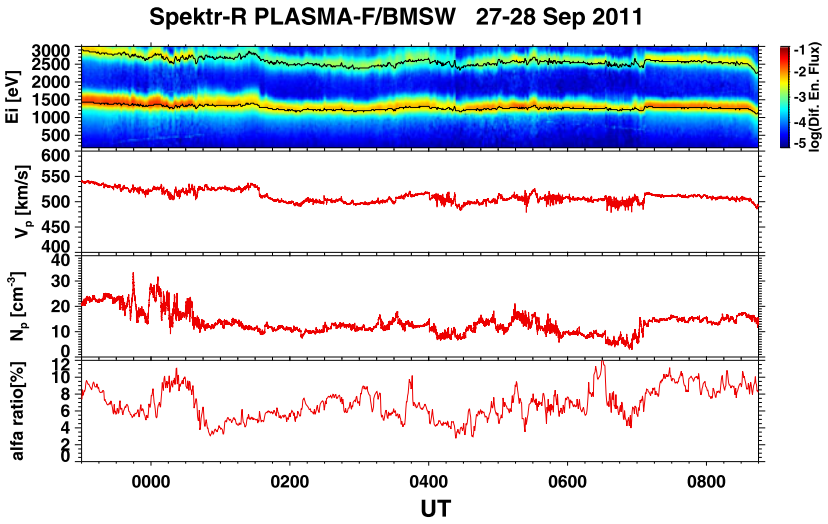


**Fig. 12** The ratio of the protons and alpha particles on September 27–28, 2011 registered by BMSW. From top to bottom: differential energy fluxes of protons and alpha particles, the total proton velocity, $V_p$; the proton density, $N_p$, and the ratio of protons and alpha particle densities

## 5 Conclusion

Taking advantage of its continuous orientation toward the Sun, the BMSW instrument determine the density, velocity, and thermal speed of the solar wind protons and alpha particles with a time resolution better than once per second. Due to a suitable Spektr-R orbit and excellent time resolution of the BMSW adaptive mode, the frequency spectra of the solar wind turbulence at MHD and ion kinetic scales can be directly measured for the first time. Furthermore, the time resolution of plasma-parameter measurements enables to detect spatial structures as small as few kilometers, thus it can contribute to unanswered questions of the fine structure, real dimensions, and oscillations associated with interplanetary shocks (bow shock), and to follow the changes of proton/alpha-particle ratios under different solar wind conditions.

In this paper, we present the basic principles of the BMSW instrument, its operation modes and demonstrate its capability to provide a comprehensive set of data. We discuss only a few of the exciting scientific questions that can be addressed with these high-time resolution ion measurements. Finally, we would like to note that the web pages of BMSW containing information on data availability and daily quick-looks can be found on: http://aurora.troja.mff.cuni.cz/spektr-r/project/.

## References

M.R. Aellig, A.J. Lazarus, J.C. Kasper, K.W. Ogilvie, Astrophys. Space Sci. **277**, 305 (2001)

L.A. Avanov et al., Kosm. Issled. **22**, 774 (1984) (in Russian)

S.D. Bale, P.J. Kellogg, F.S. Mozer, T.S. Horbury, H. Reme, Phys. Rev. Lett. (2005). doi:10.1103/PhysRevLett.94.215002

M.A. Balikhin, T.L. Zhang, M. Gedalin, N.Y. Ganushkina, S.A. Pope, Geophys. Res. Lett. (2008). doi:10.1029/2007GL032495

C.H.K. Chen, S.D. Bale, C.S. Salem, F.S. Mozer, Astrophys. J. Lett. (2011). doi:10.1088/2041-8205/737/2/L41
C.H.K. Chen, C.S. Salem, J.W. Bonnell, F.S. Mozer, S.D. Bale, Phys. Rev. Lett. (2012). doi:10.1103/PhysRevLett.109.035001
A.A. Galeev et al., Adv. Space Res. **6**(1), 45–48 (1986)
K.I. Gringauz, V.V. Bezrukikh, V.D. Ozerov, R.E. Rybchinskii, Dokl. Akad. Nauk SSSR **131**, 1301 (1960)
K.I. Gringauz, A.N. Remizov, L.I. Denscikova, T. Gombosi, I. Apati, T. Semerei, Š. Pintér, J. Šafránková, Z. Němeček, Artif. Satell. **15**, 58 (1980)
J.V. Hollweg, J. Geophys. Res. (1999). doi:10.1029/1998JA900132
P. Kajdic, X. Blanco-Cano, E. Aguilar-Rodriguez, C.T. Russell, L.K. Jian, J.G. Luhmann, J. Geophys. Res. (2012). doi:10.1029/2011JA017381
J.C. Kasper, A.J. Lazarus, J.T. Steinberg, K.W. Ogilvie, A. Szabo, J. Geophys. Res. (2006). doi:10.1029/2005JA011442
J.C. Kasper, M.L. Stevens, A.J. Lazarus, Astrophys. J. **660**, 901 (2007)
A. Koval, Z. Němeček, J. Šafránková, K. Jelínek, M. Beránek, G. Zastenker, N. Shevyrev, in *Proceedings of the Conference Solar Wind 11–SOHO 16: Connecting Sun and Heliosphere*, ESA, SP–592 (2005a), p. 681
A. Koval, J. Šafránková, Z. Němeček, Planet. Space Sci. **53**, 41 (2005b)
I. Kozák, J. Šafránková, Z. Němeček, Czechoslov. J. Phys. **35**, 568 (1985)
A.J. Lazarus, J.T. Steinberg, R.L. McNutt, in *Proceedings of the Small Instrument Workshop*, vol. 3, ed. by B.T. Tsurutani (NASA, Washington, 1993), pp. 3–11
D.J. McComas, S.J. Bame, P. Barker, W.C. Feldman, J.L. Phillips, P. Riley, J.W. Griffee, Space Sci. Rev. **86**, 563 (1998)
J.P. McFadden, C.W. Carlson, D. Larson, M. Ludlam, R. Abiad, B. Elliott, P. Turin, M. Marckwordt, V. Angelopoulos, Space Sci. Rev. (2008). doi:10.1007/s11214-008-9440-2
K.W. Ogilvie et al., Space Sci. Rev. **71**, 55 (1995)
J.J. Podesta, D.A. Roberts, M.L. Goldstein, J. Geophys. Res. (2006). doi:10.1029/2006JA011834
J.J. Podesta, J.E. Borovsky, Phys. Plasmas (2010). doi:10.1063/1.3505092
H. Reme et al., Ann. Geophys. **19**, 1303 (2001)
J. Šafránková, G. Zastenker, Z. Němeček, A. Fedorov, M. Simerský, L. Přech, Ann. Geophys. **15**, 562 (1997)
J. Šafránková, Z. Němeček, L. Přech, A. Koval, I. Čermák, M. Beránek, G. Zastenker, N. Shevyrev, L. Chesalin, Adv. Space Res. **41**, 153 (2008)
J. Šafránková, Z. Němeček, L. Přech, G.N. Zastenker, Phys. Rev. Lett. (2013). doi:10.1103/PhysRevLett.110.025004
C.S. Salem, A. Mangeney, S.D. Bale, P. Veltri, Astrophys. J. (2009). doi:10.1088/0004-637X/702/1/537
S.J. Schwartz, E. Henley, J. Mitchell, V. Krasnoselskikh, Phys. Rev. Lett. (2011). doi:10.1103/PhysRevLett.107.215002
J.T. Steinberg, A.J. Lazarus, K.W. Ogilvie, R. Lepping, J. Bymes, Geophys. Res. Lett. **23**, 1183 (1996)
O.L. Vaisberg et al., Kosm. Issled. **17**, 780 (1979) (in Russian)
V.M. Vasylinuas, *Methods of Experimental Physics*, vol. 98 (Elsevier, New York, 1971), pp. 49–88
R.T. Wicks, T.S. Horbury, C.H.K. Chen, A.A. Schekochihin, Phys. Rev. Lett. (2011). doi:10.1103/PhysRevLett.106.045001
G.N. Zastenker, Y.I. Yermolaev, Š. Pintér, Z. Němeček, J. Šafránková, A.B. Belikova, A.V. Leibov, V. Prochorenko, A.E. Stefanovitz, A.G. Bedrikov, B.T. Karimov, Adv. Space Res. **20**, 900 (1982)
G.N. Zastenker, A.O. Fedorov, Y.V. Sharko, K.A. Moldosanov, P.A. Dalin, I.P. Kirpichev, L.S. Kim, M.A. Samsonov, Adv. Space Res. **38**, 20 (2000)